Available online at www.sciencedirect.com
ScienceDirect
Trans. Nonferrous Met. Soc. China 33(2023) 3100−3112
Transactions of Nonferrous Metals Society of China
www.tnmsc.cn

Na^+-doped layered $LiNi_{1/3}Co_{1/3}Mn_{1/3}O_2$ cathode derived from low nickel matte with high structural stability and fast diffusion kinetics

Meng-chen LIAN, Qiang-chao SUN, Wei NIE, Yan-bo LIU, Tong DUAN, Hong-wei CHENG, Xiong-gang LU

State Key Laboratory of Advanced Special Steel, School of Materials Science and Engineering, Shanghai University, Shanghai 200444, China

Received 17 April 2022; accepted 15 February 2023

Abstract: Sodium ion (Na^+)-doped $Li_{1-x}Na_xNi_{1/3}Co_{1/3}Mn_{1/3}O_2$ (NCM-Na) cathode materials with enhanced stability were synthesized using a co-precipitation method. The results demonstrate the feasibility of extracting nickel from low nickel matte as a nickel source for synthetic raw materials. Subsequently, the optimal content of Na^+ is introduced in advance to occupy partially lithium-ion sites in NCM (Ni, Co, Mn) materials synthesized by chemical reagents, which achieves a stable structure with lower Li^+/Ni^{2+} mixing and improved electrochemical performance. When the dopant content of Na^+ is 1 wt.% (x=0.01), the capacity retention ratio of the produced NCM-Na cathode increases from 76.84% to 89.21% after 100 cycles (at 1C). In particular, a specific capacity of 110 $mA\cdot h\cdot g^{-1}$ is maintained after 200 cycles (at 5C). These results demonstrate that coupling materialization metallurgy and heteroatomic doping are promising strategies for the development of low-cost and high-performance $LiNi_{1/3}Co_{1/3}Mn_{1/3}O_2$ cathodes for advanced lithium-ion batteries.

Key words: lithium-ion batteries; $LiNi_{1/3}Co_{1/3}Mn_{1/3}O_2$ cathode; Na^+-doping; diffusion kinetics; low nickel matte

1 Introduction

A practical cathode material with high specific capacity and robust cyclic stability is needed to enable lithium-ion batteries (LIBs) to meet the rising requirements of the electric vehicle market [1−3]. In this sense, $LiNi_{1/3}Co_{1/3}MN_{1/3}O_2$ (NCM) cathode materials, which have low cost, high capacity, and environmental friendliness, have been considered as one of the most promising cathode candidates for high-performance LIBs [4,5]. Nevertheless, longstanding drawbacks of low electronic conductivity and in-lattice Li^+/Ni^{2+} cation mixing severely restrict their large-scale application [6].

In recent years, a vast number of strategies have been proposed to tackle these issues, including novel structural design [7−9], surface coating [10−12], and heteroatomic doping [13]. Among them, elemental doping is an efficient approach to enhance electrochemical performance by suppressing the migration of Ni^{2+} from transition metal (TM) sites to Li sites and promoting structural stability. Elements such as Na, Mg, Al, V, and Nb have been successfully introduced into the lattice structure of the NCM materials [14−16]. LI [17] studied the influence of Al doping on NCM material and showed that the bond energy of Al—O was higher than that of the Co—O, which enhances its structural stability. LV et al [13] confirmed that Nb doping could effectively reduce the degree of polarization and promote diffusion kinetics. Moreover, Nb doping facilitates the formation of an Mn^{3+}-enriched region, which is conducive to improving the electrical conductivity and electrochemical performance.

Corresponding author: Qiang-chao SUN, E-mail: Tonysun@shu.edu.cn;
Hong-wei CHENG, Tel: +86-21-66136561, E-mail: hwcheng@shu.edu.cn
DOI: 10.1016/S1003-6326(23)66320-4

Recently, LIM et al [18] reported a Na-doped Li-rich cathode material with enhanced rate capability and described the effect of Na contents on Li-ion storage. The cathode has excellent performance, with a doping content of 5 wt.%. However, although it has been confirmed that NCM cathode materials or analogues doped with Na have improved electrochemical performance, it is unclear how Na^+ doping affects the diffusion kinetics of Li^+ and subsequent electrochemical performance during the charging/discharging process in the lattice.

With the explosive growth of electric vehicles, the demand for nickel in rechargeable batteries has grown rapidly in recent years. Therefore, nickel for use in ternary cathode materials has a high cost; reserves or low nickel matte resources that have a high nickel content are abundant in China, with an output of ~200000 t/a. Cost-effective strategies to extract nickel components from low nickel matte would reduce the cost of synthesizing NCM materials, and link metallurgical technology with electrochemistry to promote the integrated utilization of nickel ore secondary resources.

To address this need, in this study, the effects of submicron NCM materials synthesized with low nickel matte leaching solution and $NiSO_4·7H_2O$ as nickel source on their electrochemical performance were investigated. Furthermore, the effects of Na dosage on the phase structure, micro-morphology, and Li^+ diffusion coefficient were explored. Moreover, Li^+ diffusion kinetics in the Na^+-doped NCM (NCM-Na) cathode was probed by applying the cyclic voltammetry (CV) and electrochemical impedance spectroscopy (EIS) techniques.

2 Experimental

2.1 Preparation of NCM and NCM-Na materials

A sulphate roasting–water leaching method was used to synchronously extract nickel, copper, and cobalt from low nickel matte. The specific steps were as follows. Low nickel matte and sodium sulfate were evenly mixed at a mass ratio of 1:0.1 and sintered for 2 h at 600 ℃ in a tube furnace. The mixture was then dissolved in 100 mL of deionized water and stirred for 2 h. The obtained filter residue was washed 3−5 times with deionized water. The resulting filtrate was transferred to a volumetric flask to obtain the leach of low nickel matte. Then, an appropriate amount of 1 mol/L sodium sulfide solution was added to remove impurity elements. The particle size distribution of the sieved low nickel matte powder used in the experiment is shown in Fig. S1 of Supporting information (SI). The chemical composition of the low nickel matte and the ICP results of the original leaching and copper removal leaching solution are shown in Tables S1 and S2 of SI, respectively. $NiSO_4·7H_2O$ and leaching solution of low nickel matte were used as nickel sources to synthesize submicron NCM materials. The obtained products were denoted as NCM-I and NCM-II, respectively.

Na-doped $Li_{1-x}Na_xNi_{1/3}Co_{1/3}Mn_{1/3}O_2$ (NCM-Na) materials were synthesized by co-precipitation method. Typically, the stoichiometric amounts of $NiSO_4·7H_2O$, $CoSO_4·6H_2O$, and $MnSO_4$ were first dissolved in deionized water to form 2 mol/L solution. Then, 2 mol/L oxalic acid solution was slowly added to the above-mixed solution under constant stirring for 4 h (40 ℃), and then centrifuged precipitate was dried to form a pinkish-white precipitate at 80 ℃ for 12 h. After that, the obtained powders were calcined at 450 ℃ in the air for 6 h to get a precursor. It was then mixed with a certain amount of $LiOH·H_2O$ and NaOH by grinding and calcined at 500 ℃ for 6 h in the air to obtain the pre-calcined product. Finally, the target product of $Li_{1-x}Na_xNi_{1/3}Co_{1/3}Mn_{1/3}O_2$ (NCM-Na; x=0, 0.005, 0.01, 0.02, 0.03, 0.04) was obtained by calcinating at 850 ℃ for 15 h in the air. The XRD patterns and SEM images show that the materials feature an obvious layered structure and spheroidal particle morphology, and the surface is smooth, indicating that samples with improved crystallinity are obtained (as shown in Figs. S2−S5 of SI). The NCM materials were synthesized by the same process but without NaOH addition.

2.2 Material characterizations

X-ray diffraction (XRD) was executed on a Bruker D8 Advance with Cu K_α radiation (λ= 0.154 nm) to identify the crystalline phase of the as-synthesized samples. The XRD patterns were collected in a range of 2θ from 10° to 80° with a step size of 0.02°. The morphologies and elemental distributions of the as-prepared samples were observed by scanning electron microscopy (SEM) and energy-dispersive X-ray spectrometry (EDS, JEOL, JSM−7500F). The valence states of nickel, cobalt, manganese, and sodium were examined by

the X-ray photoelectron spectroscopy (XPS, ESCALAB 250Xi). The peak processing was conducted using the XPS Peak 4.1 Program.

2.3 Electrochemical measurements

The CR-2016-coin cells composed of the NCM(-Na) cathode, Li metal anode, and a polymer separator (Celgard 2400) were used for the electrochemical measurements. The electrolyte consisted of 1 mol/LLiPF$_6$ dissolved in ethylene carbonate and diethyl carbonate at 1:1 (volume ratio). The as-prepared active materials were mixed with acetylene black and polyvinylidene fluoride (PVDF) binder (8:1:1, mass ratio) in N-methyl-2-pyrrolidone (NMP) solvent to form a homogenous slurry. The slurry was coated on aluminum foil and dried in a vacuum at 80 ℃ for 12 h. It was then press punched into 12 mm-diameter disks. Galvanostatic charge/discharge cycling was performed on Land Test System (CT−2001A) within 2.8−4.3 V range. The cyclic voltammogram (CV) tests were carried out with an electrochemical workstation (Versa STAT 3) at various scanning rates and electrochemical impedance spectroscopy (EIS) tests were conducted in the frequency range from 0.01 to 100 kHz with an amplitude of 5 mV.

3 Results and discussion

3.1 Effect of nickel source on NCM cathodes

The XRD patterns of the NCM-I and NCM-II are shown in Figs. 1(a, b), respectively. A low degree of Li/Ni mixing is observed ($I_{(003)}/I_{(104)}$>1.2), which is favourable for good electrochemical performance. Two pairs of split peaks ((006/102) and (108/110)) suggest that the material has a prominent layered structure. However, the (003) peak of NCM-II shifts to a lower angle (Fig. 1(b)), which may be related to the trace Fe and Cu impurities contained in the leaching solution.

Figures 1(c, d) show the SEM images of the NCM-I and NCM-II prepared by calcination at 850 ℃ for 15 h, respectively. Both samples present wafer-like morphology, with no obvious difference

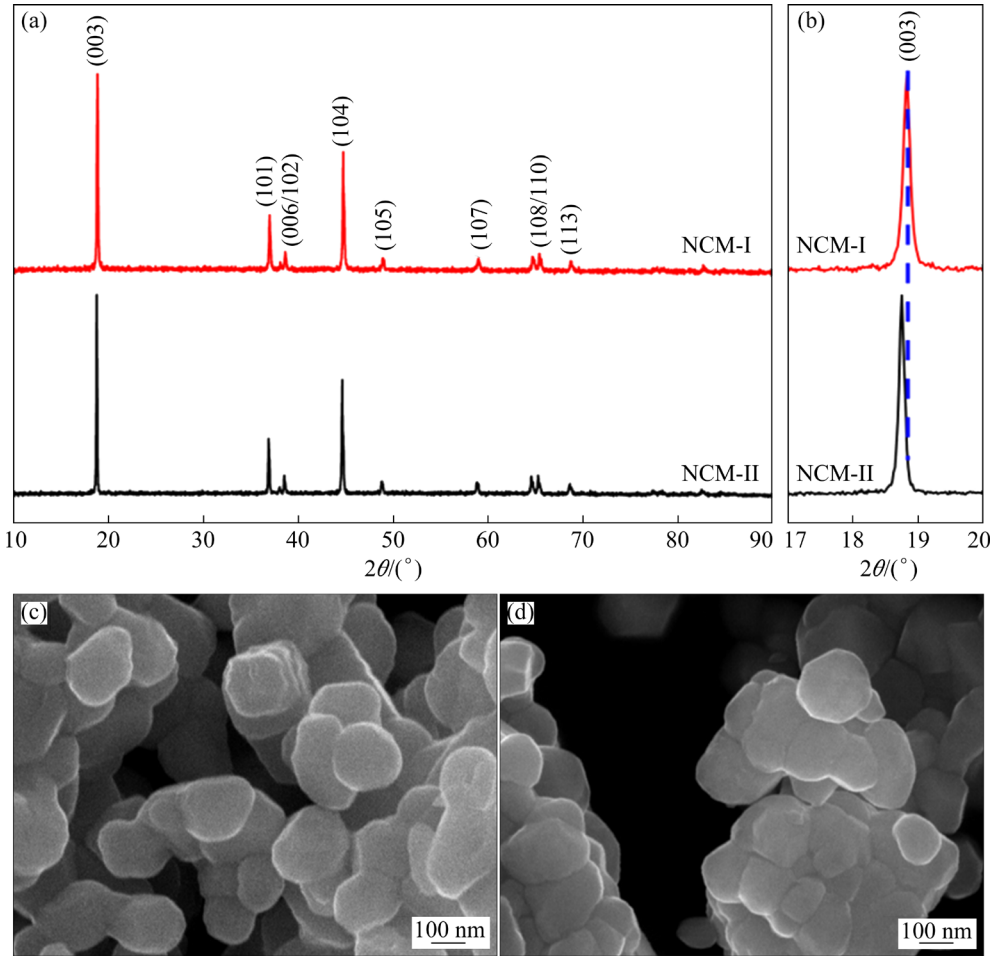

Fig. 1 XRD patterns of NCM-I (a) and NCM-II (b) and SEM images of NCM-I (c) and NCM-II (d) at 850 ℃ for 15 h

in morphology or particle size. These results reveal that the $LiNi_{1/3}Co_{1/3}Mn_{1/3}O_2$ material with a well-layered structure can be prepared by using the leaching solution from low nickel matte as the nickel source. Figure S6 in SI shows the EDS spectra and corresponding elemental mapping of the NCM-I and NCM-II. The Ni, Co, Mn, and O in NCM-I are uniformly distributed in the selected area. Figures S6(g−l) show not only the uniform distribution of Ni, Co, and Mn, but also the uniform distribution of Cu and Fe elements, which might be attributed to the trace impurity contents in the leaching solution.

Figure 2(a) illustrates the cycling performance of the NCM-I and NCM-II cathodes at a current density of 1*C*. The initial discharge capacity of two materials is 143 $mA·h·g^{-1}$, and the capacity retention rate is ~77.3% after 100 cycles. There is no significant difference in the cycling performance of the two materials at low current density.

Figure 2(b) shows the rate performances of NCM-I and NCM-II cathodes at various current densities. At 0.1*C*, the specific discharge capacities of the two materials are around 164.7 and 159.9 $mA·h·g^{-1}$, respectively. In addition, the specific reversible capacities are similar at 0.5*C*, 1*C*, and 2*C*. However, specific discharge capacity of the NCM-I cathode maintains at 110 $mA·h·g^{-1}$ at 5*C*, while that of the NCM-II cathode is only 0.8 $mA·h·g^{-1}$. This shows that the electrochemical performance of the NCM-II cathode is close to that of the NCM-I cathode at relatively low current densities, but there is almost no discharge capacity at higher current density (over 5*C*), which should originate from the effects of Fe and Cu impurities in low nickel matte. Based on previous reports, Cu impurities may generate the trace of the Li_2CuO_2 phase, which is an inactive material for Li^+ diffusion, resulting in inferior charge–discharge capacity at high current density. Moreover, Fe impurities reduce the conductivity of lithium ions [19,20].

The CV curves of the NCM-I and NCM-II cathodes at a scan rate of 0.1 mV/s are displayed in Figs. 3(a, b), respectively. During the first three

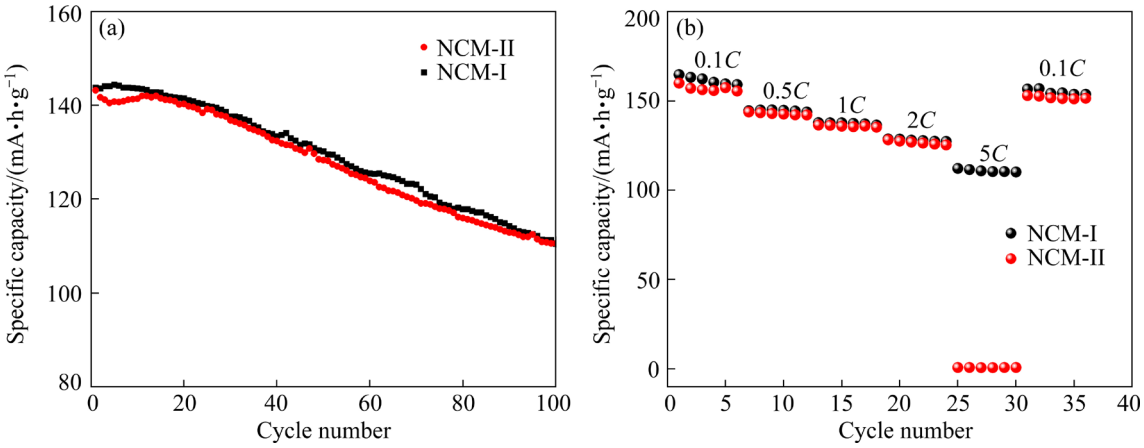

Fig. 2 Cycle performance (a) and rate performance (b) of NCM-I and NCM-II cathodes

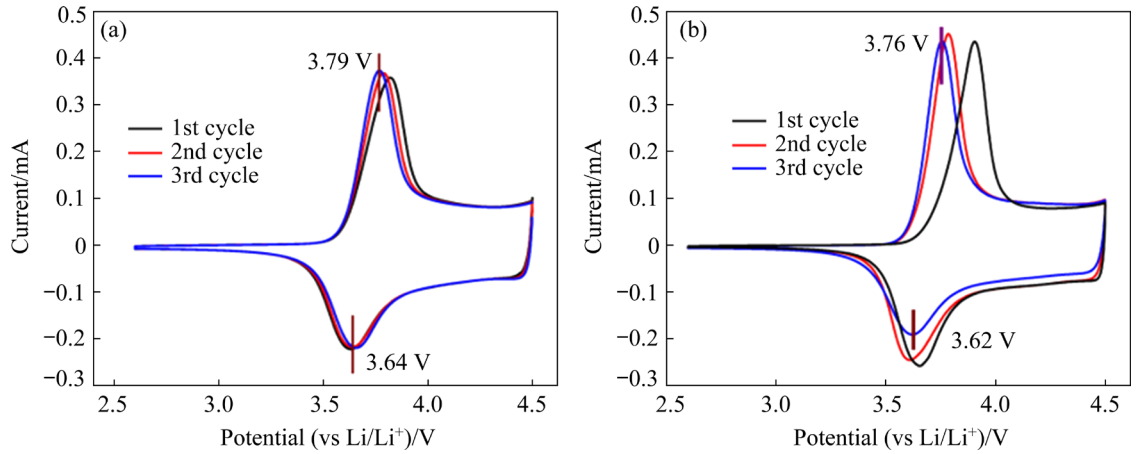

Fig. 3 CV curves of NCM-I (a) and NCM-II (b) in voltage windows of 2.8−4.3 V at scan rate of 0.1 mV/s

cycles, a pair of redox peaks of two materials appear at 3.79/3.64 and 3.76/3.62 V, corresponding to the redox reaction of Ni^{2+}/Ni^{4+}. Moreover, the potential difference of the corresponding redox peak could reflect the polarization degree of the material [21]. The potential differences of the NCM-I and NCM-II cathodes are 0.15 and 0.14 V, respectively, indicating a similar degree of polarization. The curves of NCM-I cathode have high coincidence, which confirms that NCM-I electrode possesses better cyclic reversibility. The NCM-II cathode exhibits an inferior coincidence, which agrees with the results of electrochemical performance [22].

To assess the stability of NCM materials in the calcination process, high-temperature in-situ XRD tests were conducted, and the results are shown in Fig. 4.

At the beginning, the temperature increased from 30 to 50 ℃ and then continuously increased to 600 ℃; XRD patterns were recorded every 50 ℃.

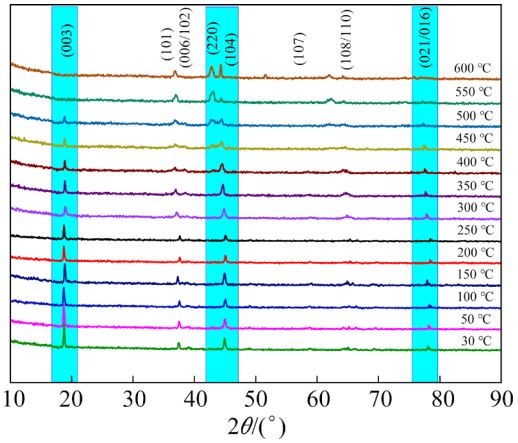

Fig. 4 High-temperature in-situ XRD patterns of NCM-I electrode

The results reveal that the $I(003)/I(104)$ ratio does not change significantly from 30 to 250 ℃, which means that Ni^{2+} is not replaced by Li^{+}, and the original hexagonal layered structure is maintained. However, the (003) peak intensity and $I(003)/I(104)$ ratio decrease significantly from 250 to 500 ℃. At 500−600 ℃, the (003) diffraction peak disappears, indicating that the hexagonal layered structure is transformed into the spinel structure ($Fd\overline{3}m$) [23]. The (220) peak appears gradually on the left side of the (104) peak from 450 ℃, and is assigned to metallic nickel. The appearance of this peak reflects a transition of the layered structure into the rock-salt phase ($Fm\overline{3}m$). This evolution from layered structure to spinel and rock-salt phase structure suggests that the structural stability of the NCM material needs to be further improved. Therefore, to further improve the performance of these materials, a sodium doping strategy was employed to enhance their stability. Additionally, more efforts should be devoted to synthesizing NCM materials via low nickel matte leaching solution; this is considered a potential research direction to achieve low-cost preparation of ternary cathode materials.

3.2 Microstructure and electrochemical performance of NCM-Na cathodes

The XRD patterns of the NCM-Na with different Na^{+} doping amounts are illustrated in Fig. 5, and the Rietveld refinement result of the NCM-Na sample with 1 wt.% dopant content (x=0.01) is shown in Fig. S7 of SI. All diffraction peaks are well indexed to the α-$NaFeO_2$ type layered structure with the $R\overline{3}m$ space group.

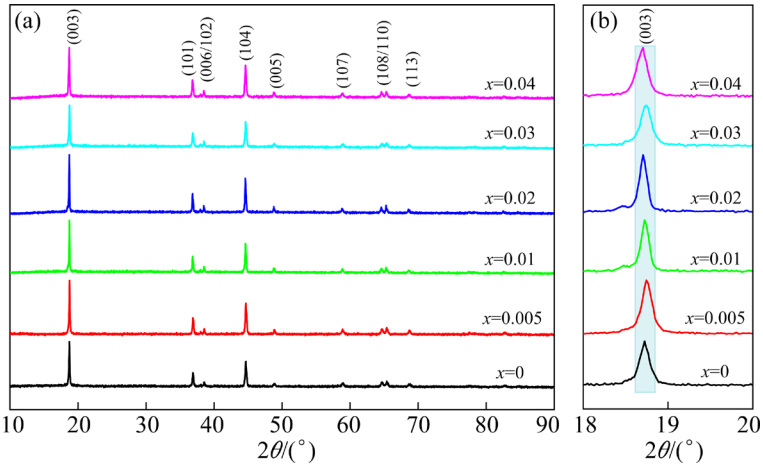

Fig. 5 XRD patterns of NCM-Na materials with different Na^{+} doping amounts

Compared with the NCM sample, no impurity peaks are detected in NCM-Na sample, indicating that Na^+ doping cannot change the original crystal structure. Two pairs of (006)/(102) and (008)/(110) diffraction peaks are split obviously, implying that the samples possess a well-formed layered structure in the lattice [6,24]. The (003) peak of the NCM-Na sample shifts slightly to a lower angle with increasing Na doping amount (Fig. 5(b)). This indicates that the *c*-axis lattice constants increase. As shown in Table S3 of SI, it is more intuitive to observe that the *a*-axis and *c*-axis lattice parameters increase with the increase in doping amount, which enlarges the interlayer spacing of the NCM lattice with the doping of Na^+. The increased *c*-axis lattice constant reflects the expansion of the Li interlayer spacing, which suggests that the (de)intercalation kinetics of Li^+ is promoted. Besides, the intensity ratio of the (003)/(104) peaks is the largest when the doping amount is 1 wt.%. The ratio has a downward trend with increasing doping amount, demonstrating that the samples exhibit a lower cation mixing degree and better lattice structure when x=0.01 [25].

Figure 6 shows the XPS spectra of the NCM and NCM-Na (x=0.01) samples. Ni, Co, and Mn are observed in the full spectrum (Figs. 6(a, b)). The binding energies of Ni $2p_{3/2}$, Co $2p_{3/2}$, and Mn $2p_{3/2}$ are located at 855, 780, and 643 eV, respectively, fitting well with the oxidation states of Ni^{2+}, Co^{3+}, and Mn^{4+}, respectively, which is consistent with previous reports [26,27]. A weaker peak of Na 1s is also observed at a binding energy of around 1070.0 eV in the Na-doped sample (Fig. 6(c)), confirming that the Na element is successfully doped into the NCM samples. Figures 6(d–f) show that the binding energies of $2p_{3/2}$ peaks of Ni, Co, and Mn in both samples are close, while the NCM-Na sample possesses a higher peak intensity, implying that the doping of Na can enhance the lattice strength. Figure 6(g–i) show the peak fitting spectra of NCM-Na (x=0.01) sample. In Fig. 6(g),

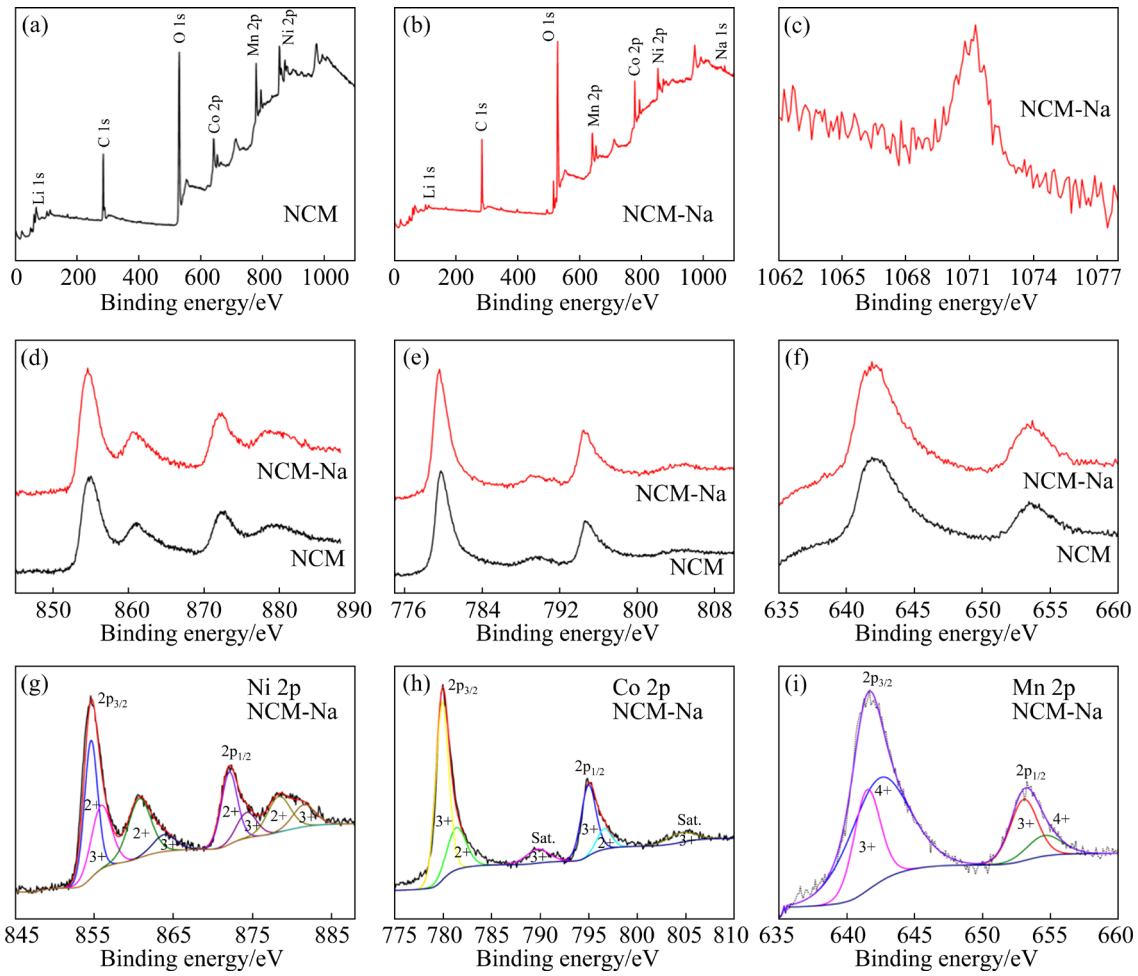

Fig. 6 XPS full spectra of NCM (a), NCM-Na (b), Na 1s (c), Ni 2p (d), Co 2p (e), Mn 2p (f), and high-resolution XPS spectra of NCM-Na material for Ni 2p (g), Co 2p (h), and Mn 2p (i)

the major strong peaks at 854.58 and 872.38 eV correspond to Ni $2p_{3/2}$ and Ni $2p_{1/2}$, respectively; oscillation peaks at 860.58 and 880.08 eV are also observed, which proves the existence of Ni^{2+} [28,29]. The minor peaks at 855.98 and 874.38 eV can be obtained by Gaussian fitting, indicating the existence of a small amount of Ni^{3+}. The small amounts of Ni^{3+} and Mn^{3+} ions may be caused by the electron transfer between Mn^{4+} and Ni^{2+}, owing to valency degeneracy through the dynamic equilibrium ($Mn^{4+}+Ni^{2+}\rightarrow Mn^{3+}+Ni^{3+}$) [30]. As shown in Fig. 6(h), the Co $2p_{3/2}$ and Co $2p_{1/2}$ peaks at 779.98 and 794.88 eV are in agreement with the Co^{3+} species. The binding energies of Mn $2p_{3/2}$ and Mn $2p_{1/2}$ are at 642.08 and 653.78 eV, respectively (Fig. 6(i)), which fits well with the Mn^{4+}. Minor peaks at around 641.0 and 653 eV are ascribed to Mn^{3+} in the Mn 2p spectrum [31,32].

The SEM images and EDS mappings of the NCM-Na samples with different Na^+ doping amounts are shown in Fig. 7. The particle size increases from 100 to 500 nm with the increase of Na^+ content, and the size distributions of all samples exhibit different uniformities. The sample with x=0.01 shows a moderate particle size and better consistency, which is more conducive to the (de)intercalation of Li^+. Moreover, even distributions of Ni, Co, Mn, and Na are observed in elemental mapping. Accordingly, Na^+-doped NCM cathodes with optimized content are prepared successfully.

Long-cycle and rate capability performances of NCM-Na cathode are shown in Fig. 8. The initial discharge capacity of all samples (x=0, 0.005, 0.01, 0.02, 0.03, and 0.04) at 1C (1C=160 mA·h·g^{-1}) are 143.8, 142.9, 152.9, 149.6, 146, and 145.5 mA·h·g^{-1}, respectively. After 100 cycles, the capacity retention rates are approximately 76.84%, 90.34%, 89.21%, 86.7%, 90.40%, and 85.15%, respectively (Fig. 8(a)).

The cycle performance at a higher rate (5C) is depicted in Fig. 8(b). The pristine NCM cathode shows an initial capacity of 126.8 mA·h·g^{-1}, which is lower than that of doped samples with different doping contents (129.1, 133.6, 139.8, 123.1, and 125.6 mA·h·g^{-1}, respectively). In particular, the cathode material with x=0.01 achieves the highest capacity retention (87.42%) even after 200 cycles, which can mainly be attributed to doped Na^+ occupying the position of Li^+, resulting in the enlargement of Li plane layers and facilitation of (de)intercalation kinetics of Li^+ in the bulk [33,34]. Therefore, the reversible capacity and cycling stability are improved. The rate capability of all samples is shown in Fig. 8(c). The NCM-Na electrode with x=0.01 has better rate capability in terms of capacity recovery rate and stability; the corresponding charge–discharge curves at different

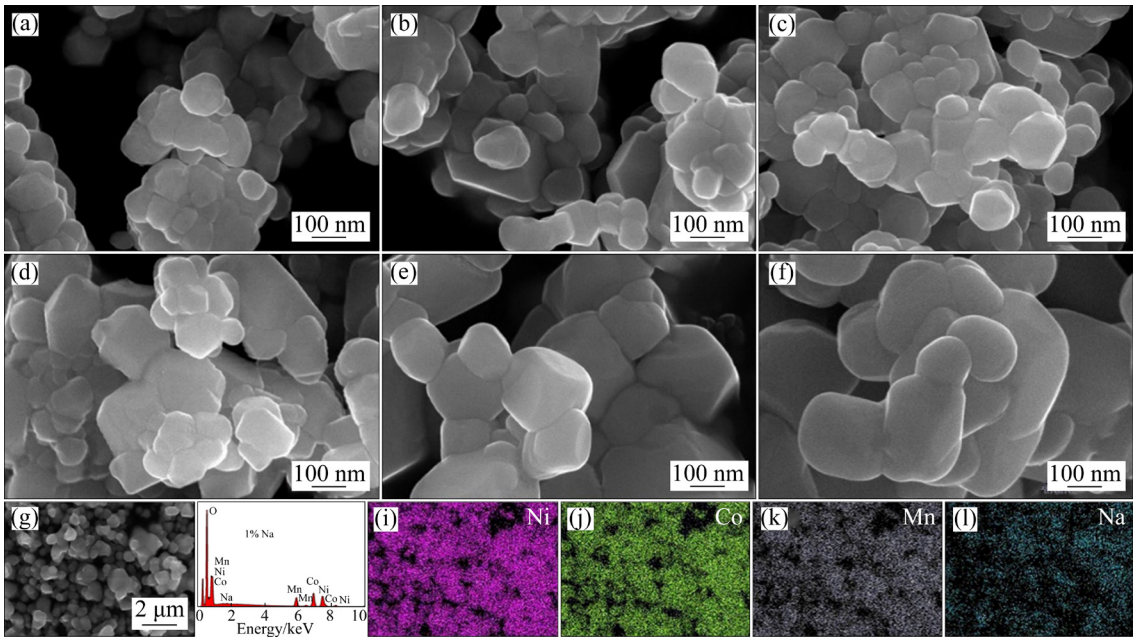

Fig. 7 SEM images of NCM-Na with different Na^+ doped amounts (a−f); SEM image (g), EDS pattern (h) and corresponding element distribution mappings (i−l) of x=0.01 sample (g, h): (a) x=0; (b) x=0.005; (c) x=0.01; (d) x=0.02; (e) x=0.03; (f) x=0.04

rates are shown in Fig. S8 of SI. Moreover, even at higher current density (5*C* or 10*C*), it still achieves 124.3 and 109.2 mA·h·g^{-1} reversible capacity, while the pristine one only maintains at 112.2 and 93.5 mA·h·g^{-1}. Figures 8(d−f) show the charge and discharge voltage curves of NCM-Na samples at 1*C* during the 1st, 50th, and 100th cycles. The NCM cathode exhibits the highest charging plateau and lowest discharge plateau, suggesting more serious electrode polarization [35,36]. In contrast, the lowest charging platform and highest discharge platform show the lowest polarization of x=0.01 sample during the cycle. The electrochemical performance of the NCM-Na cathode with x=0.01 in comparison with previous works is given in Table 1.

3.3 Kinetics analysis

Cyclic voltammetry (CV) tests were carried out to study the redox reaction mechanism of the

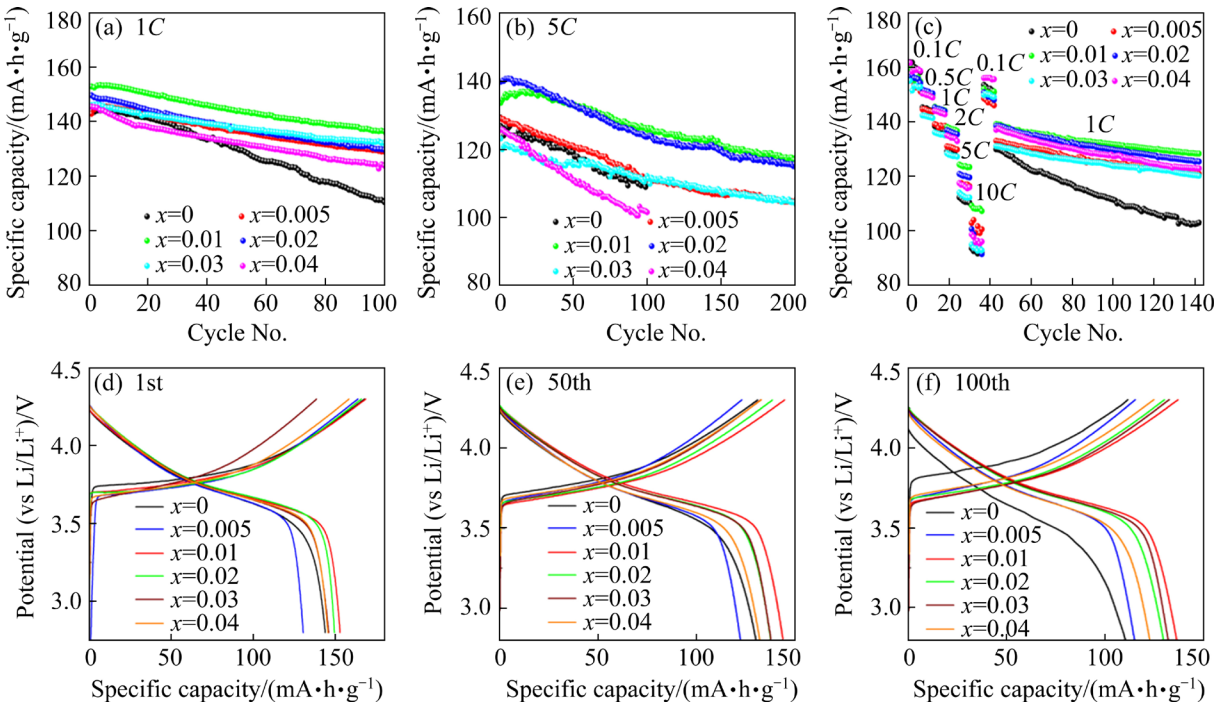

Fig. 8 Cycle performance at 1*C* (a) and 5*C* (b), rate capability (c), and charge−discharge curves at 1*C* of NCM-Na electrode (d−f)

Table 1 Comparison with previously-reported NCM cathodes with different dopant elements

Material	Current density	Potential range/V	Initial capacity/(mA·h·g^{-1})	Cycle number	Capacity retention/%	Source
$LiNi_{1/3}Co_{1/3}Mn_{1/3-0.02}Mg_{0.02}O_2$	0.2*C*	2.5−4.3	~164	50	89.40	Ref. [37]
$LiNi_{0.33}Co_{0.33}Mn_{0.31}Nb_{0.02}O_2$	1*C*	2.7−4.3	170.6	100	89	Ref. [13]
$LiNi_{1/3-x}Co_{1/3}Mn_{1/3}Cu_xO_2$	0.2*C*	2.5−4.5	178	100	80.30	Ref. [38]
$LiNi_{1/3}Co_{1/3}Mn_{1/3}Fe_xO_2$	1*C*	3.0−4.3	~145	100	86.60	Ref. [39]
Ti-doped $LiNi_{1/3}Co_{1/3}Mn_{1/3}O_2$	0.2*C*	2.6−4.4	130.4	−	−	Ref. [25]
$NaNi_{1/3}Mn_{1/3}Co_{1/3}O_2$	0.1*C*	2.0−4.0	~139	50	85	Ref. [40]
B_2O_3-modified $LiNi_{1/3}Co_{1/3}Mn_{1/3}O_2$	2*C*	3.0−4.5	~105	100	86	Ref. [41]
W-doped $LiNi_{1/3}Co_{1/3}Mn_{1/3}O_2$	1*C*	2.7−4.3	~160	50	91	Ref. [42]
$LiNi_{1/3}Co_{1/3}Mn_{1/3}O_2$ derived spent lithium-ion batteries	1*C*	2.7−4.3	145.2	200	85.90	Ref. [43]
Na-doped $LiNi_{1/3}Co_{1/3}Mn_{1/3}O_2$	1*C*	2.6−4.5	152.9	100	86.70	This work
	5*C*		133.6	200	87.40	

NCM and NCM-Na cathodes at a scan rate of 0.1 mV/s. As shown in Fig. 9, all materials contain a pair of redox peaks, which is ascribed to the redox reaction of Ni^{2+}/Ni^{4+} during the charge and discharge process [44]. During the first three cycles, the oxidation peak potential of the NCM cathode shifts from 3.83 to 3.79 V due to the activation of the cathode material surface in the initial charge–discharge process. The NCM-Na cathode with x=0.01 dopant content keeps excellent coincidence, suggesting an increase in the electrochemical reversibility and structural stability. Besides, the potential differences of redox peaks for different materials are 0.14, 0.08, 0.09, 0.03, 0.09 and 0.12 V, respectively. Generally, the smaller the potential difference is, the lower the polarization degree of cathodes is, indicating that the polarization degree of the Na-doped material has been significantly reduced [41,45].

CV measurements at different scanning rates were performed for the NCM-Na and NCM samples to compare the diffusion kinetics of Li^+. The results are illustrated in Fig. 10. As the scanning rate increases, the oxidation peak moves to a higher potential, and the reduction peak shifts to a lower potential, which means that the degree of electrode polarization increases. Moreover, the NCM-Na cathode displays a sharper

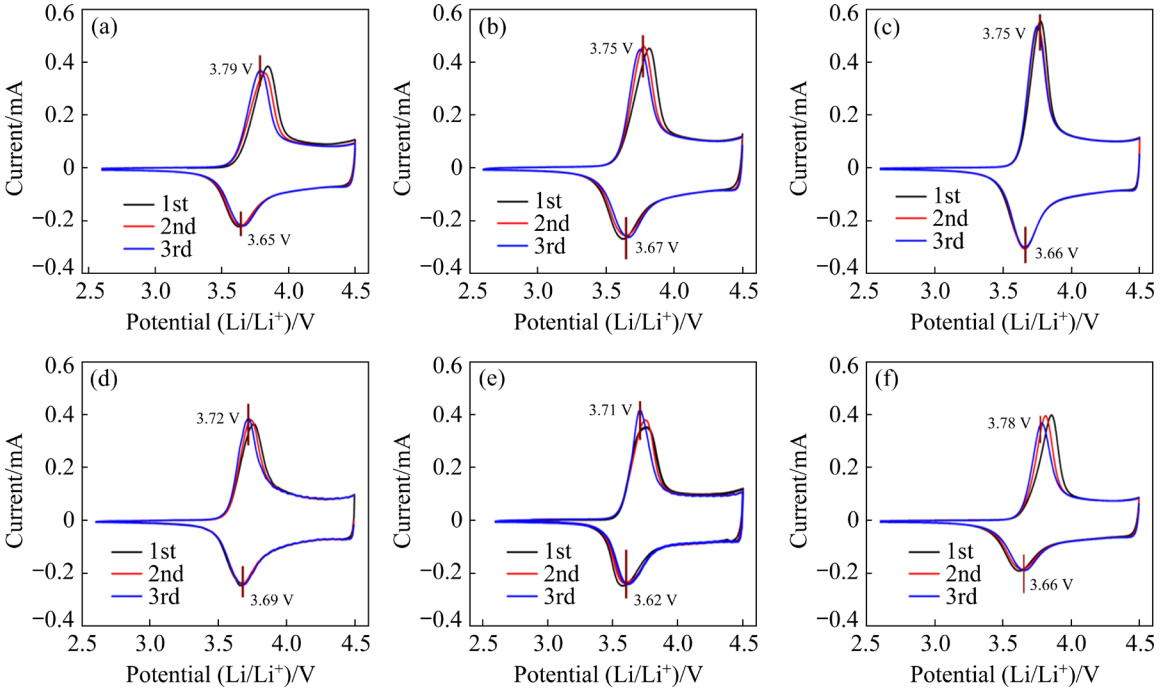

Fig. 9 Cyclic voltammetry (CV) profiles of NCM-Na cathodes: (a) x=0; (b) x=0.005; (c) x=0.01; (d) x=0.02; (e) x=0.03; (f) x=0.04

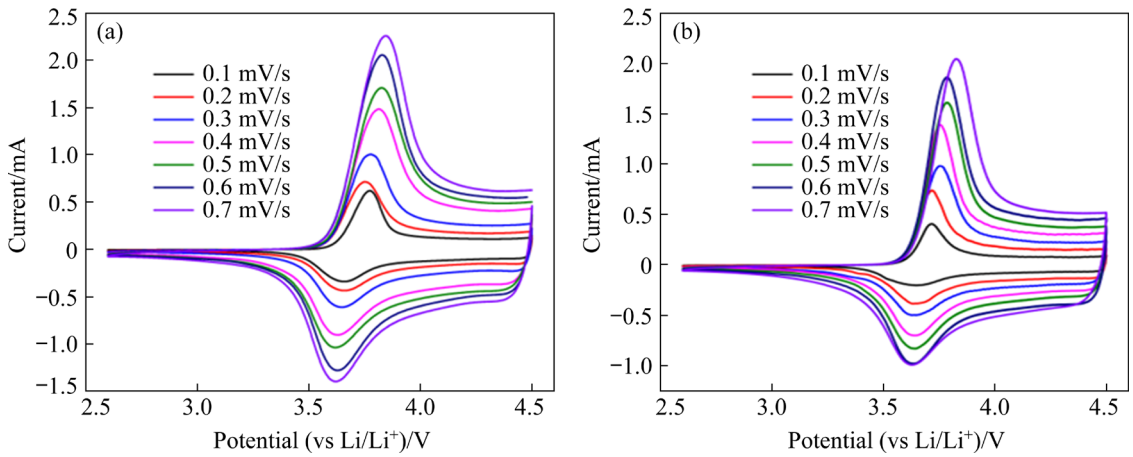

Fig. 10 Cyclic voltammetry (CV) profiles of NCM-Na (a), and NCM (b) at different scan rates from 0.1 to 0.7 mV/s

peak shape than pristine NCM, suggesting faster Li^+ (de)intercalation kinetics in the NCM-Na cathode, which is consistent with the results of rate performance tests.

The relationship between the scan rate and peak current is shown in Fig. 11(a). The linear relationship suggests that the electrochemical reaction is a typical diffusion-controlled process. Accordingly, the Li^+ diffusion coefficient (D^+_{Li}) can be calculated based on the Randles–Sevcik formula [46]:

$$I_p = 2.6\times10^5 n^{3/2} A D^{1/2}_{Li^+} v^{1/2} C_{Li^+} \quad (1)$$

where I_p is the peak current, n is the number of electrons involved in the redox reaction (n=1), A is the electrode surface area, D^+_{Li} is the lithium-ion diffusion rate, v is the scan rate, and C^+_{Li} is the molar concentration of electrode lithium ions (6.02×10^2 mol/mL). The D^+_{Li} values of the NCM material in the oxidation and reduction processes are 2.67×10^{-11} and 6.73×10^{-12} cm^2/s, respectively, which are lower than those of the NCM-Na (2.8×10^{-11} and 1.2×10^{-11} cm^2/s), indicating that the

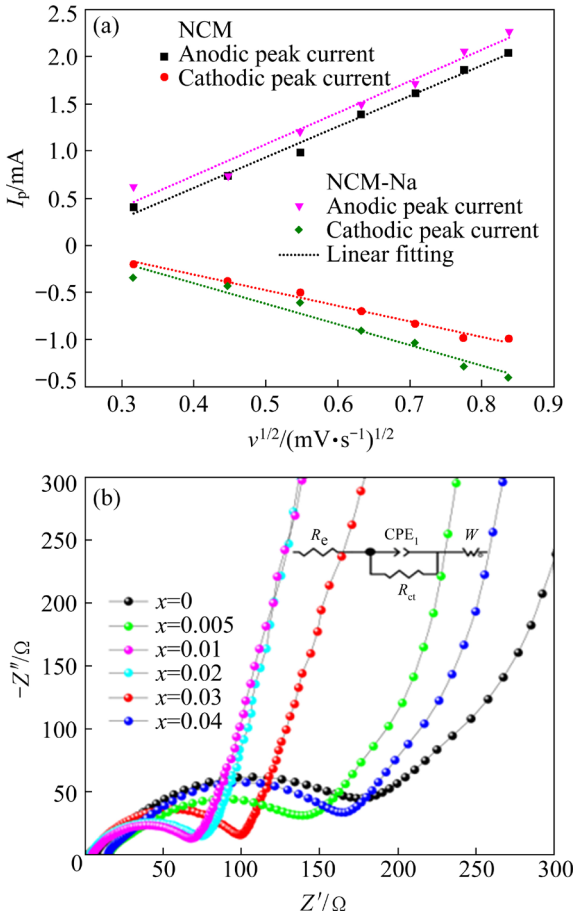

Fig. 11 Relationship plots between scan rate and peak current (a) and EIS profiles of all samples (b)

Na^+-doped sample with x=0.01 can promote the diffusion kinetics of electrode reactions.

The EIS spectra of the NCM and NCM-Na materials before cycling are shown in Fig. 11(b). The curves of all materials are characterized by two depressed semicircles and a long slope. The semicircular in the middle-frequency region is assigned to the solid electrolyte mesophase resistance (R_e) and charge transfer resistance (R_{ct}), and the slope in the low-frequency region corresponds to the Warburg impedance (W) [41]. The results obtained by fitting the equivalent circuit are shown in Table S4 of SI. The R_{ct} of doped materials is lower than that of pristine NCM. The minimum charge transfer resistance of the x=0.01 sample is 59.82 Ω·cm^2, which is much lower than that of pristine materials. Those findings reveal that NCM-Na materials have higher reactivity, implying that Na^+ doping can enhance the reaction kinetics, improving rate performance and cycling stability.

4 Conclusions

(1) Nickel extracted from low nickel matte is a feasible resource for the preparation of NCM cathode materials, which promotes the comprehensive utilization of nickel ore secondary resources. However, the obtained cathode shows inferior rate capability at a high current density (5C).

(2) NCM-Na cathodes with $NiSO_4·7H_2O$ as the nickel source were synthesized by the conventional co-precipitation method. NCM-Na cathode with 1 wt.% Na^+ doped amount has the best performance. The initial discharge capacity is as high as 152.9 mA·h·g^{-1} and capacity retention approaches 89.21% after 100 cycles at 1C.

(3) The intercalation of Na^+ with optimized content can enlarge the Li slab distance and stabilize the layered structure of the NCM-Na cathode, resulting in improved cycling stability and rate capability. These findings provide a promising way to enhance structural stability and lower the synthetic cost of NCM-type cathode materials.

Acknowledgments

This work was supported by the National Natural Science Foundation of China (Nos. 51874196, 51674164), the Program for Professor of Special Appointment at the Shanghai Institutions of

Higher Learning, China (No. TP2020032), the Iron and Steel Joint Research Fund of the National Natural Science Foundation of China and China Baowu Steel Group Corp. Ltd. (No. U1860203), the Independent Research and Development Project of State Key Laboratory of Advanced Special Steel, Shanghai Key Laboratory of Advanced Ferrometallurgy, Shanghai University, China (No. SKLASS 2021-Z03), and the Science and Technology Commission of Shanghai Municipality, China (Nos. 21DZ1208900, 19DZ2270200, 20511107700)

Supporting information

Supporting information in this paper can be found at: http://tnmsc.csu.edu.cn/download/16-p3100-2022-0476-Supporting_Information.pdf.

References

[1] ZHU Li-min, BAO Chen-guang, XIE Ling-ling, YANG Xin-li, CAO Xiao-yu. Review of synthesis and structural optimization of $LiNi_{1/3}Co_{1/3}Mn_{1/3}O_2$ cathode materials for lithium-ion batteries applications [J]. Journal of Alloys and Compounds, 2020, 831: 154864.

[2] SUN Zhong-hui, LI Zheng, GAO Li-fang, ZHAO Xin, HAN Dong-xue, GAN Shi-yu, GUO Shao-jun, NIU Li. Grafting benzenediazonium tetrafluoroborate onto $LiNi_xCo_yMn_zO_2$ materials achieves subzero-temperature high-capacity lithium-ion storage via a diazonium soft-chemistry method [J]. Advanced Energy Materials, 2019, 9: 1802946.

[3] LU Shi-jie, LIU Yang, HE Zhen-jiang, LI Yun-jiao, ZHENG Jun-chao, MAO Jing, DAI Ke-hua. Synthesis and properties of single-crystal Ni-rich cathode materials in Li-ion batteries [J]. Transactions of Nonferrous Metals Society of China, 2021, 31: 1074−1086.

[4] XU Ya-di, ZHANG Jun, WU Zhen-guo, XU Chun-liu, LI Yong-chun, XIANG Wei, WANG Yuan, ZHONG Yan-jun, GUO Xiao-dong, CHEN Hong. Stabilizing the structure of nickel-rich lithiated oxides via Cr doping as cathode with boosted high-voltage/temperature cycling performance for Li-ion battery [J]. Energy Technology, 2020, 8: 1900498.

[5] LIU Peng, RU Qiang, WANG Zhen, WANG Bei, GUO Qing, ZHANG Peng, HOU Xian-hua, SU Shi-chen. Harnessing the synergic lithium storage and morphology evolution of 1D bundle-like $NiCo_2O_4$@TiO_2 hybrid to prolong the cycling life for lithium ion batteries [J]. Chemical Engineering Journal, 2018, 350: 902−910.

[6] CHEN Jia-wei, XING Li-dan, YANG Xue-rui, LIU Xiang, LI Tie-jun, LI Wei-shan. Outstanding electrochemical performance of high-voltage $LiNi_{1/3}Co_{1/3}Mn_{1/3}O_2$ cathode achieved by application of $LiPO_2F_2$ electrolyte additive [J]. Electrochimica Acta, 2018, 290: 568−576.

[7] ZHAO Na, CHEN Jian, LIU Zhong-qing, BAN Ke-jian, DUAN Wen-jun. Porous $LiNi_{1/3}Co_{1/3}Mn_{1/3}O_2$ microsheets assembled with single crystal nanoparticles as cathode materials for lithium ion batteries [J]. Journal of Alloys and Compounds, 2018, 768: 782−788.

[8] CHEN Zhen, CHAO Dong-liang, CHEN Ming-hua, SHEN Ze-xiang. Hierarchical porous $LiNi_{1/3}Co_{1/3}Mn_{1/3}O_2$ with yolk–shell-like architecture as stable cathode material for lithium-ion batteries [J]. RSC Advances, 2020, 10: 18776−18783.

[9] XU Chun-liu, XIANG Wei, WU Zhen-guo, XU Ya-di, LI Yong-chun, LI Hong-tai, XIAO Yao, TAN Bo-chuan, GUO Xiao-dong, ZHONG Ben-he. Hierarchical hollow structured lithium nickel cobalt manganese oxide microsphere synthesized by template-sacrificial route as high performance cathode for lithium ion batteries [J]. Journal of Alloys and Compounds, 2019, 777: 434−442.

[10] ZOU Tong, QI Wei-jing, LIU Xiao-shuo, WU Xiao-qin, FAN Ding-huan, GUO Shou-hui, WANG Li. Improvement of the electrochemical performance of $Li_{1.2}Ni_{0.13}Co_{0.13}Mn_{0.54}O_2$ cathode material by Al_2O_3 surface coating [J]. Journal of Electroanalytical Chemistry, 2020, 859: 113845.

[11] WANG Xin-zhi, JIANG Qian-qian, ZHANG Yi-chi, YUAN Nan-nan, TANG Jian-guo. High efficient and environment friendly plasma-enhanced synthesis of Al_2O_3-Coated $LiNi_{1/3}Co_{1/3}Mn_{1/3}O_2$ with excellent electrochemical performance [J]. Frontiers in Chemistry, 2020, 8: 72.

[12] LV Fan, CHENG Hong-wei, NIE Wei, SUN Qiang-chao, LIU Yan-bo, DUAN Tong, XU Qian, LU Xiong-gang. Enhancing rate capacity and cycle stability of $LiNi_{1/3}Co_{1/3}$-$Mn_{1/3}O_2$ cathode material by laminar V_2O_5 coating for lithium-ion batteries [J]. ChemistrySelect, 2021, 6: 6339−6347.

[13] LV Cong-jie, YANG Jing, PENG Yi, DUAN Xiao-chuan, MA Jian-min, LI Qiu-hong, WANG Tai-hong. 1D Nb-doped $LiNi_{1/3}Co_{1/3}Mn_{1/3}O_2$ nanostructures as excellent cathodes for Li-ion battery [J]. Electrochimica Acta, 2019, 297: 258−266.

[14] SUN Qiang-chao, CHENG Hong-wei, ZHAO Kang-ning, ZHOU Hui-jie, ZHAO Hong-bin, YAO Wen-li, XU Qian, LU Xiong-gang. Mg^{2+} doped $LiNi_{1/3}Co_{1/3}Mn_{1/3}O_2$ hollow flake-like structures with enhanced performances cathodes for Lithium–ion batteries [J]. ChemistrySelect, 2020, 5: 1275−1281.

[15] LI Fang-cheng, ZHANG Gang, ZHANG Zong-liang, YANG Jian, LIU Fang-yang, JIA Ming, JIANG Liang-xing. Regeneration of Al-doped $LiNi_{0.5}Co_{0.2}Mn_{0.3}O_2$ cathode material by simulated hydrometallurgy leachate of spent lithium-ion batteries [J]. Transactions of Nonferrous Metals Society of China, 2022, 32: 593−603.

[16] HU Xia, GUO Hua-jun, PENG Wen-jie, WANG Zhi-xing, LI Xin-hai, HU Qi-yang. Effects of Nb doping on the performance of $0.5Li_2MnO_3{\cdot}0.5LiNi_{1/3}Co_{1/3}Mn_{1/3}O_2$ cathode material for lithium-ion batteries [J]. Journal of Electro-analytical Chemistry, 2018, 822: 57−65.

[17] LI Zhu-yuan. The improvement for the electrochemical performances of $LiNi_{1/3}Co_{1/3}Mn_{1/3}O_2$ cathode materials for Lithium-ion batteries by both the Al-doping and an advanced synthetic method [J]. International Journal of Electro-chemical Science, 2019, 14: 3524−3534.

[18] LIM S N, SEO J Y, JUNG D S, AHN W, SONG H S, YEON S H, PARK S B. Rate capability for Na-doped $Li_{1.167}Ni_{0.18}$-

$Mn_{0.548}Co_{0.105}O_2$ cathode material and characterization of Li-ion diffusion using galvanostatic intermittent titration technique [J]. Journal of Alloys and Compounds, 2015, 623: 55−61.

[19] JO M, PARK S, SONG J, KWON K. Incorporation of Cu into $Li[Ni_{1/3}Co_{1/3}Mn_{1/3}]O_2$ cathode: Elucidating its electrochemical properties and stability [J]. Journal of Alloys and Compounds, 2018, 764: 112−121.

[20] KAZUAKI A, MITSUHARU T, HIRONORI K, HIROYUKI K, OSAMU N, YUKISHIGE I, RYOJI K, MASARU T, YASUO T. Preparation of $LiFeO_2$ with alpha-$NaFeO_2$-type structure using a mixed-alkaline hydrothermal method [J]. Journal of the Electrochemical Society, 1997, 144: L177.

[21] LIU, Xi-zheng, LI Hui-qiao, ISHIDA M, ZHOU Hao-shen. PEDOT modified $LiNi_{1/3}Co_{1/3}Mn_{1/3}O_2$ with enhanced electrochemical performance for lithium ion batteries [J]. Journal of Power Sources, 2013, 243: 374−380.

[22] HU Guo-rong, ZHANG Man-fang, LIANG Long-wei, PENG Zhong-dong, DU Ke, CAO Yan-bing. Mg−Al−B co-substitution $LiNi_{0.5}Co_{0.2}Mn_{0.3}O_2$ cathode materials with improved cycling performance for lithium-ion battery under high cutoff voltage [J]. Electrochimica Acta, 2016, 190: 264−275.

[23] BAK S M, HU En-yuan, ZHOU Yong-ning, YU Xi-qian, SENANAYAKE S D, CHO S J, KIM K B, CHUNG K Y, YANG Xiao-qing, NAM K W. Structural changes and thermal stability of charged $LiNi_xMn_yCo_zO_2$ cathode materials studied by combined in situ time-resolved XRD and mass spectroscopy [J]. ACS Applied Materials & Interfaces, 2014, 6: 22594−22601.

[24] DENG Chao, ZHANG Sen, FU Bing-lei, YANG Sai-yu, MA Lei. Synthetic optimization of nanostructured $Li[Ni_{1/3}Mn_{1/3}Co_{1/3}]O_2$ cathode material prepared by hydroxide coprecipitation at 273 K [J]. Journal of Alloys and Compounds, 2010, 496: 521−527.

[25] LI Guang-yin, HUANG Zhen-lei, ZUO Zi-cheng, ZHANG Zhan-jun, ZHOU Heng-hui. Understanding the trace Ti surface doping on promoting the low temperature performance of $LiNi_{1/3}Co_{1/3}Mn_{1/3}O_2$ cathode [J]. Journal of Power Sources, 2015, 281: 69−76.

[26] WANG Qi, LAI Yan-qing, LIU Fang-yang, JIANG Liang-xing, JIA Ming, WANG Xi-lun. Sb_2S_3 nanorods/ porous-carbon composite from natural stibnite ore as high-performance anode for lithium-ion batteries [J]. Transactions of Nonferrous Metals Society of China, 2021, 31: 2051−2061.

[27] SINHA N N, MUNICHANDRAIAH N. Synthesis and characterization of carbon-coated $LiNi_{1/3}Co_{1/3}Mn_{1/3}O_2$ in a single step by an inverse microemulsion route [J]. ACS Applied Materials & Interfaces, 2009, 1: 1241−1249.

[28] JIANG Qian-qian, LANG Peng, LI Jie, TANG Jian-guo. Improving the elevated-temperature behaviors of $LiNi_{1/3}Co_{1/3}Mn_{1/3}O_2$ by surface modification with nano−La_2O_3 [J]. Journal of Alloys and Compounds, 2018, 742: 549−554.

[29] JIANG Qian-qian, YUAN Nan-nan, ZHANG Yi-chi, TANG Jian-guo. Surface nano-ZnO doped $LiNi_{1/3}Co_{1/3}Mn_{1/3}O_2$ for an improved elevated temperature performance by a facile low-temperature solid-state process [J]. Ionics, 2019, 25: 4523−4530.

[30] LIAN Fang, GAO M, QIU W H, AXMANN P, WOHLFAHRT M M. Fe-doping effects on the structural and electrochemical properties of $0.5Li_2MnO_3{\cdot}0.5LiMn_{0.5}Ni_{0.5}O_2$ electrode material [J]. Journal of Applied Electrochemistry, 2012, 42: 409−417.

[31] JIN Yan-ling, HUO Mei-xia, REN Fang, REN Peng-gang. In situ thermally reduced graphene oxide enhancing lithium storage of $0.3Li_2MnO_3{\cdot}0.7LiNi_{1/3}Co_{1/3}Mn_{1/3}O_2$ cathode material [J]. Journal of Energy Storage, 2019, 26: 100953.

[32] CHEN Yu, ZHAO Wei-min, ZHANG Quan-hai, YANG Guang-zhi, ZHENG Jian-ming, TANG Wei, XU Qun-jie, LAI Chun-yan, YANG Jun-he, PENG Cheng-xin. Armoring $LiNi_{1/3}Co_{1/3}Mn_{1/3}O_2$ cathode with reliable fluorinated organic–inorganic hybrid interphase layer toward durable high rate battery [J]. Advanced Functional Materials, 2020, 30: 2000396.

[33] GONG Chun-xia, LV Wei-xin, QU Li-min, BANKOLE O E, LI Guang-hua, ZHANG Rui, HU Meng, LEI Li-xu. Syntheses and electrochemical properties of layered $Li_{0.95}Na_{0.05}Ni_{1/3}Co_{1/3}Mn_{1/3}O_2$ and $LiNi_{1/3}Co_{1/3}Mn_{1/3}O_2$ [J]. Journal of Power Sources, 2014, 247: 151−155.

[34] HE Wei, YUAN Ding-ding, QIAN Jiang-feng, AI Xin-ping, YANG Han-xi, CAO Yu-liang. Enhanced high-rate capability and cycling stability of Na-stabilized layered $Li_{1.2}[Co_{0.13}Ni_{0.13}Mn_{0.54}]O_2$ cathode material [J]. Journal of Materials Chemistry A, 2013, 1: 11397−11403.

[35] WANG Wan-lin, YIN Zhou-lan, WANG Jia-pei, WANG Zhi-xing, LI Xin-hai, GUO Hua-jun. Effect of heat-treatment on Li_2ZrO_3-coated $LiNi_{1/3}Co_{1/3}Mn_{1/3}O_2$ and its high voltage electrochemical performance [J]. Journal of Alloys and Compounds, 2015, 651: 737−743.

[36] ZHANG Lu-lu, WANG Ji-qing, YANG Xue-lin, LIANG Gan, LI Tao, YU Peng-lin, MA Di. Enhanced electrochemical performance of fast ionic conductor $LiTi_2(PO_4)_3$-coated $LiNi_{1/3}Co_{1/3}Mn_{1/3}O_2$ cathode material [J]. ACS Applied Materials & Interfaces, 2018, 10: 11663−11670.

[37] ZHU Ji-ping, YAN Jia-wei, ZHANG Lei. High specific capacity Mg-doping $LiNi_{1/3}Co_{1/3}Mn_{1/3}O_2$ cathode materials synthesised by a simple stepwise co-precipitation method [J]. Micro & Nano Letters, 2019, 14: 129−132.

[38] YANG Li, REN Feng-zhang, FENG Qi-gao, XU Guang-ri, LI Xiao-bo, LI Yuan-chao, ZHAO Er-qing, MA Jing-jing, FAN Shu-min. Effect of Cu doping on the structural and electrochemical performance of $LiNi_{1/3}Co_{1/3}Mn_{1/3}O_2$ cathode materials [J]. Journal of Electronic Materials, 2018, 47: 3996−4002.

[39] PARK S, KIM D, KU H, JO M, KIM S, SONG J, YU J, KWON K. The effect of Fe as an impurity element for sustainable resynthesis of $Li[Ni_{1/3}Co_{1/3}Mn_{1/3}]O_2$ cathode material from spent lithium-ion batteries [J]. Electrochimica Acta, 2019, 296: 814−822.

[40] NGUYEN V H, NGUYEN L M, HUYNH T T K, TRAN V M, LE M L P. New sodium intercalation cathode prepared by sodiation of delithiated host $LiNi_{1/3}Co_{1/3}Mn_{1/3}O_2$ [J]. Advances in Materials Science and Engineering, 2021, 2021: 6280582.

[41] LI Jun-hao, LIU Zhong-qi, WANG Yi-fan, WANG Rui-gang. Investigation of facial B_2O_3 surface modification effect on

the cycling stability and high-rate capacity of $LiNi_{1/3}Co_{1/3}Mn_{1/3}O_2$ cathode [J]. Journal of Alloys and Compounds, 2020, 834: 155150.

[42] LI Pei-yao, HUANG Ying-de, TANG Lin-bo, WEI Han-xin, FU Hao, HE Zhen-jiang, ZHENG Jun-chao. W-doped $LiNi_{1/3}Co_{1/3}Mn_{1/3}O_2$ with excellent high-rate performance synthesized via hydrothermal lithiation [J]. Journal of the Electrochemical Society, 2022, 169: 050509.

[43] FAN Xiao-ping, SONG Chun-hong, LU Xi-fei, SHI Ying, YANG Sheng-long, ZHENG Feng-hua, HUANG You-guo, LIU Kui, WANG Hong-qiang, LI Qing-yu. Separation and recovery of valuable metals from spent lithium-ion batteries via concentrated sulfuric acid leaching and regeneration of $LiNi_{1/3}Co_{1/3}Mn_{1/3}O_2$ [J]. Journal of Alloys and Compounds, 2021, 863: 158775.

[44] LUO Zhi-mei, SUN Yan-guang, LIU Hui-yong. Electrochemical performance of a nano SnO_2-modified $LiNi_{1/3}Co_{1/3}Mn_{1/3}O_2$cathode material [J]. Chinese Chemical Letters, 2015, 26: 1403−1408.

[45] ZHOU Hui-jie, CHENG Hong-wei, ZHAO Hong-bin, ZHAO Kang-ning, ZHAO Yu-feng, ZHANG Jiu-jun, XU Qian, LU Xiong-gang. Superior stability and dynamic performance of single crystal $LiNi_{1/3}Co_{1/3}Mn_{1/3}O_2$ nanorods from β-MnO_2 template for Lithium-ion batteries [J]. Journal of the Electrochemical Society, 2019, 166: A59−A67.

[46] LI Qi, LI Guang-she, FU Chao-chao, LUO Dong, FAN Jian-ming, LI Li-ping. K^+-doped $Li_{1.2}Mn_{0.54}Co_{0.13}Ni_{0.13}O_2$: A novel cathode material with an enhanced cycling stability for Lithium-ion batteries [J]. ACS Applied Materials & Interfaces, 2014, 6: 10330−10341.

低冰镍衍生的具有高结构稳定性和快速扩散动力学的钠离子掺杂层状 $LiNi_{1/3}Co_{1/3}Mn_{1/3}O_2$ 正极

练梦晨，孙强超，聂 薇，刘岩博，段 彤，程红伟，鲁雄刚

上海大学 材料科学与工程学院 高品质特殊钢冶金与制备省部共建国家重点实验室，上海 200444

摘 要：通过共沉淀法合成钠离子(Na^+)掺杂的高稳定性 $Li_{1-x}Na_xNi_{1/3}Co_{1/3}Mn_{1/3}O_2$(NCM-Na)正极材料。首先论证采用低冰镍提取镍作为合成材料镍源的可行性。其次，在化学试剂合成的 NCM(Ni, Co, Mn)材料中预先引入最优含量的 Na^+，占据部分 Li^+位点，实现具有更低 Li^+/Ni^{2+}阳离子混排的稳定结构，从而提高其电化学性能。结果表明，当 Na^+掺杂量为 1%(质量分数)(x=0.01) 时，获得的 NCM-Na 正极材料在 1C 电流密度下，循环 100 次后容量保持率从 76.84%提高至 89.21%。特别是在 5C 大电流密度下，循环 200 次后，可逆放电比容量依然维持在 110 mA·h·g^{-1}。这为杂原子掺杂耦合材料化冶金开发低成本、高性能锂离子电池三元 $LiNi_{1/3}Co_{1/3}Mn_{1/3}O_2$ 正极材料提供具有前景的策略。

关键词：锂离子电池；$LiNi_{1/3}Co_{1/3}Mn_{1/3}O_2$ 正极；钠离子掺杂；扩散动力学；低冰镍

(Edited by Bing YANG)